nature chemistry

ARTICLES

PUBLISHED ONLINE: 6 JUNE 2016 | DOI: 10.1038/NCHEM.2536

Self-assembled molecular p/n junctions for applications in dye-sensitized solar energy conversion

Byron H. Farnum, Kyung-Ryang Wee and Thomas J. Meyer*

The achievement of long-lived photoinduced redox separation lifetimes has long been a central goal of molecular-based solar energy conversion strategies. The longer the redox-separation lifetime, the more time available for useful work to be extracted from the absorbed photon energy. Here we describe a novel strategy for dye-sensitized solar energy applications in which redox-separated lifetimes on the order of milliseconds to seconds can be achieved based on a simple toolkit of molecular components. Specifically, molecular chromophores (C), electron acceptors (A) and electron donors (D) were self-assembled on the surfaces of mesoporous, transparent conducting indium tin oxide nanoparticle (nanoITO) electrodes to prepare both photoanode (nanoITO|–A–C–D) and photocathode (nanoITO|–D–C–A) assemblies. Nanosecond transient-absorption and steady-state photolysis measurements show that the electrodes function microscopically as molecular analogues of semiconductor p/n junctions. These results point to a new chemical strategy for dye-sensitized solar energy conversion based on molecular excited states and electron acceptors/donors on the surfaces of transparent conducting oxide nanoparticle electrodes.

At the heart of semiconductor photovoltaic devices is the light-driven formation and separation of an electron/hole (e^-/h^+) pair at a p/n junction[1]. Molecular analogues of the semiconductor p/n junction have been investigated both in solution and on surfaces using dyads and triads of molecular chromophores (C) chemically linked to spatially separated electron acceptors (A) and/or donors (D)[2–10]. In appropriately designed assemblies, excitation of the chromophore and sequential electron transfer results in a redox-separated (RS) state, $A–C–D + h\nu \rightarrow A^-–C–D^+$, with transient free energy stored as the difference in redox potentials between the $A^{0/-}$ and $D^{+/0}$ couples. The molecular nature of the p/n junction analogue and the ability to make changes by chemical synthesis provide a basis for controlling both the magnitude of the transiently stored energy and the intra-assembly electron-transfer dynamics. Examples have been reported for which the lifetime of the RS state in a fluid solution, dictated by back-electron transfer, $A^-–C–D^+ \rightarrow A–C–D$, occurs on the microseconds timescale[5–7,11].

Exploitation of the molecular p/n junction concept in an energy-conversion device is facilitated by transfer of the assembly to a conductive electrode surface[12–14]. We report here the application of a systematic self-assembly approach on transparent conductive indium tin oxide nanoparticle (nanoITO) electrodes with a high surface area. These electrodes mimic the size, mesoporous morphology and surface areas of nanocrystalline TiO_2 electrodes used in dye-sensitized solar cells. The high surface area available within films of multiple micrometres thickness allows for the binding of thousands of molecular assemblies with a high visible-light absorptivity. The high conductivity and visible transparency of the nanoITO electrodes make them ideal substrates for investigating the electrochemical, photochemical and photophysical properties of surface-bound molecules and assemblies[15–20].

The self-assembly strategy adopted here is based on a facile layer-by-layer procedure with Zr^{IV}–phosphonate bridging between redox-active units developed by Mallouk and co-workers[21,22] as well as by other groups[14,23–26]. Recently, this approach was used for the preparation of chromophore–catalyst assemblies on mesoporous TiO_2 for applications in dye-sensitized photoelectrosynthesis cells[27,28]. Here we describe an application in which the excitation of designed assemblies that consist of molecular chromophores, donors and acceptors is used to generate controlled redox potential gradients for directing the flow of light-driven intra-assembly electron transfer. By varying the order of addition of individual molecular units to the nanoITO surface, we prepared a molecular photoanode with light-driven electron-transfer reactions directed towards the electrode surface, and a photocathode with electron-transfer reactions directed away from the electrode surface.

Visible-light excitation of the photoanode assemblies resulted in interfacial RS states that lasted for milliseconds to seconds, depending on the applied potential, which are competitive with the interfacial RS state lifetimes observed for dye-sensitized TiO_2 and core–shell SnO_2–TiO_2 photoanodes[29–31]. Comparative measurements for the photocathode assemblies revealed interfacial RS lifetimes in the millisecond range, which far surpass any previous report of photoinduced redox separation for dye-sensitized NiO photocathodes[32–36]. The strategy presented here therefore represents a simple modular method for producing long-lived photoanodic and photocathodic redox separation driven by molecular components, without the use of traditional wide-bandgap semiconductors.

Results and discussion

Idealized representations of the molecular p/n junction analogues investigated here are illustrated in Fig. 1. The Ru^{II} polypyridyl-based chromophore ($[Ru^{II}(4,4'\text{-}(PO_3H_2)_2\text{-}2,2'\text{-bipyridine})_2(2,2'\text{-bipyridine})](Cl)_2$ (RuP_2^{2+})), methyl viologen-based electron acceptor ($[N,N'\text{-}((CH_2)_2PO_3H_2)_2\text{-}4,4'\text{-bipyridinium}](PF_6)_2$ (MV^{2+})) and dianiline-based electron donor ($N,N,N',N'\text{-}((CH_2)_3PO_3H_2)_4\text{-}4,4'\text{-}$dianiline (DA)) were synthesized and characterized by established literature procedures[14,37,38]. The multiple phosphonate groups of each molecular species enabled attachment to the oxide surface of nanoITO and assembly formation by using Zr^{IV} bridging.

Department of Chemistry, University of North Carolina at Chapel Hill, Chapel Hill, North Carolina 27599-3290, USA. *e-mail: tjmeyer@unc.edu

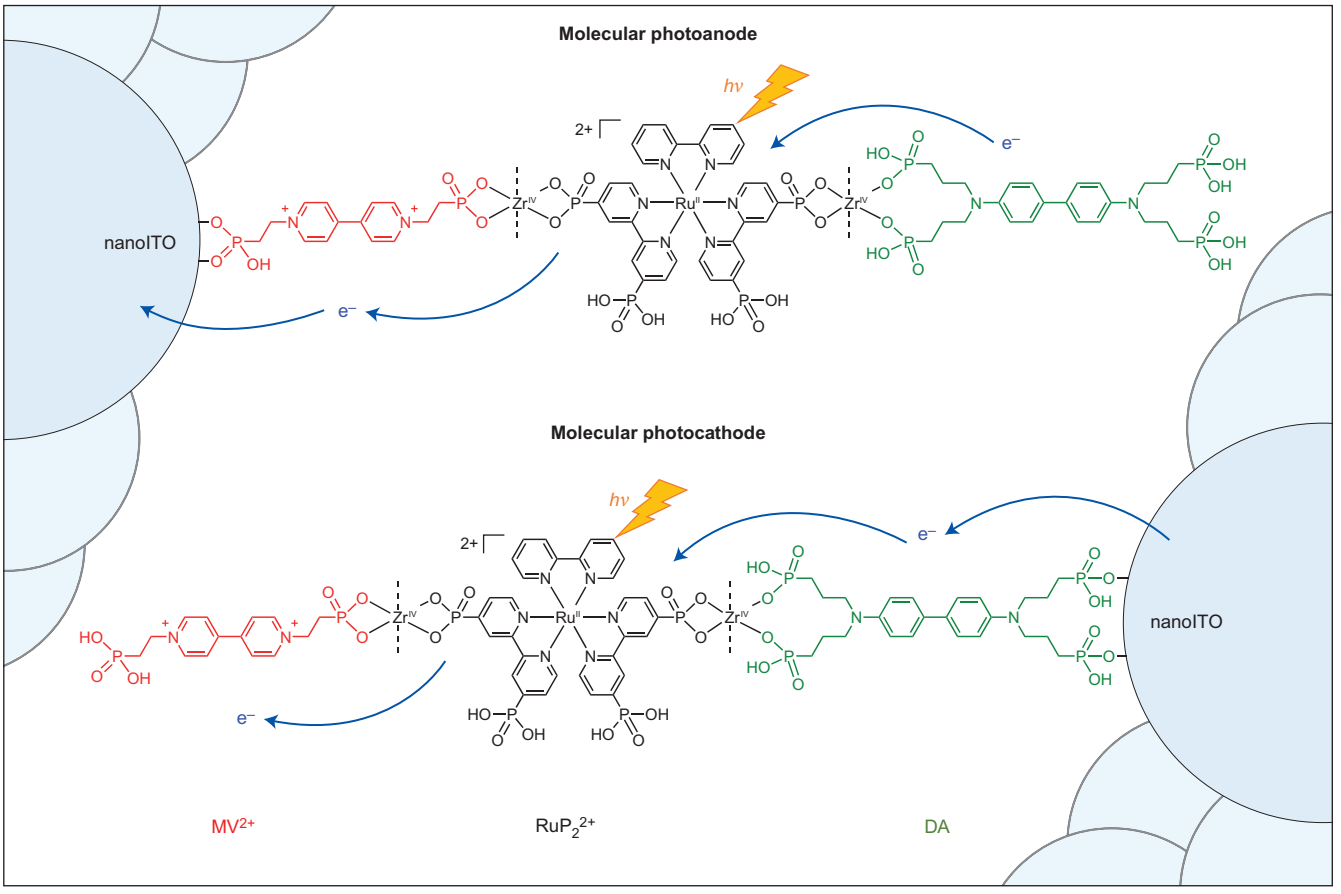

Figure 1 | Layer-by-layer molecular p/n junction assemblies on mesoporous nanoITO electrodes. Molecular photoanodes (top) and photocathodes (bottom) were constructed from individual molecular chromophores (RuP_2^{2+}), electron acceptors (MV^{2+}) and electron donors (DA) on the surface of nanoITO electrodes. Arrows show the direction of light-driven electron-transfer reactions in each assembly.

Mesoporous 2.5 μm thick nanoITO films of 10–20 nm particles were deposited onto conductive fluorine-doped tin oxide glass as reported previously[17]. Assemblies were prepared on the surface of nanoITO by soaking the electrodes in 0.1 M $HClO_4$ aqueous solutions that contained either 0.1 mM RuP_2^{2+} (12 hours), 1.2 mM MV^{2+} (12 hours), 2.8 mM DA (12 hours) or, for Zr^{IV} bridging, 6 mM $ZrOCl_2{\cdot}8H_2O$ (two hours) in sequential order for the indicated times to give complete surface coverage. Photoanode assemblies were synthesized in the order nanoITO + MV^{2+} + Zr^{IV} + RuP_2^{2+} + Zr^{IV} + DA to give nanoITO|–MV^{2+}–RuP_2^{2+}–DA (Zr^{IV} is removed for clarity). Photocathodes were derivatized in the reverse order to give nanoITO|–DA–RuP_2^{2+}–MV^{2+}.

Spectroelectrochemical measurements on the individual RuP_2^{2+}, MV^{2+} and DA components derivatized individually on nanoITO (that is, nanoITO|–RuP_2^{2+} and so on) were carried out in acetonitrile (MeCN) with 0.1 M $LiClO_4$ or 0.1 M $TBAClO_4$ (tetrabutylammonium perchlorate) electrolytes to evaluate formal reduction potentials (versus Ag/AgCl) and spectral properties of oxidized/reduced forms. Table 1 provides a summary of the formal reduction potentials measured as the applied potential (E_{app}) at which half of the total spectral change associated with reduction/oxidation had occurred (see the Supplementary Information for further details). For nanoITO|–RuP_2^{2+}, metal-based oxidative ($E^{o\prime}(RuP_2^{3+/2+}) = 1.30$ V) and ligand-based reductive ($E^{o\prime}(Ru^{2+/+}) = -1.30$ V) redox couples were observed, consistent with previous reports[38]. Molar absorptivity spectra for surface-bound –RuP_2^{3+}, –RuP_2^{2+} and –RuP_2^{+} are shown in Fig. 2a (inset). Reduction potentials for the surface-bound metal-to-ligand charge-transfer (MLCT) excited state –$RuP_2^{2+\star}$ ($[Ru^{III}(4,4'\text{-}(PO_3H_2)_2\text{-}bpy^{\bullet-})\ (4,4'\text{-}(PO_3H_2)_2\text{-}bpy)(bpy)]^{2+\star}$) were calculated from the excited-state free energy above the ground state, $\Delta G_{es} = 2.14$ eV (Supplementary Fig. 8), and the expressions $E^{o\prime}(RuP_2^{3+/2+\star}) = E^{o\prime}(RuP_2^{3+/2+}) - \Delta G_{es}$ and $E^{o\prime}(RuP_2^{2+\star/+}) = E^{o\prime}(RuP_2^{2+/+}) + \Delta G_{es}$.

For nanoITO|–MV^{2+}, reversible $MV^{2+/+\bullet}$ and $MV^{+\bullet/0}$ couples appeared at $E^{o\prime} = -0.46$ and -0.90 V, respectively. The molar absorptivity spectrum for surface-bound –$MV^{+\bullet}$ is shown in Fig. 2a and includes characteristic absorption features at $\lambda_{max} = 400$ nm ($\varepsilon = 33{,}900\ M^{-1}\ cm^{-1}$) and 600 nm ($\varepsilon = 12{,}900\ M^{-1}\ cm^{-1}$), consistent with previous reports[39]. Reversible reduction potentials for the $DA^{+\bullet/0}$ and $DA^{2+/+}$ couples for nanoITO|–DA were $E^{o\prime} = 0.49$ and 0.76 V, respectively. Figure 2a shows the molar absorptivity spectrum for surface-bound –$DA^{+\bullet}$, which has principal features at $\lambda_{max} = 475$ ($\varepsilon = 11{,}400\ M^{-1}\ cm^{-1}$) and 1,000 nm ($\varepsilon = 11{,}200\ M^{-1}\ cm^{-1}$).

Figure 2b shows ultraviolet–visible (UV-vis) spectra for the complete photoanode assembly, nanoITO|–MV^{2+}–RuP_2^{2+}–DA, measured in a three-electrode photoelectrochemical cell in MeCN with 0.1 M $LiClO_4$ at $E_{app} = -0.4$, 0.0 and 0.5 V vs Ag/AgCl. The MLCT absorption feature for –RuP_2^{2+}– at $\lambda_{max} = 465$ nm ($\varepsilon = 16{,}400\ M^{-1}\ cm^{-1}$) appears in all three spectra. The surface

Table 1 | Formal reduction potentials.

MV^{2+}			RuP_2^{2+}				DA	
	+•/0	2+/+•	2+/+†	2+*/+	3+/2+*	3+/2+	+•/0	2+/+•
$E^{o\prime}$	−0.90	−0.46	−1.30	0.84	−0.84	1.30	0.49	0.76

Surface bound redox potentials measured on nanoITO electrodes and reported as V vs Ag/AgCl at room temperature in MeCN with 0.1 M $LiClO_4$. †0.1 M $TBAClO_4$.

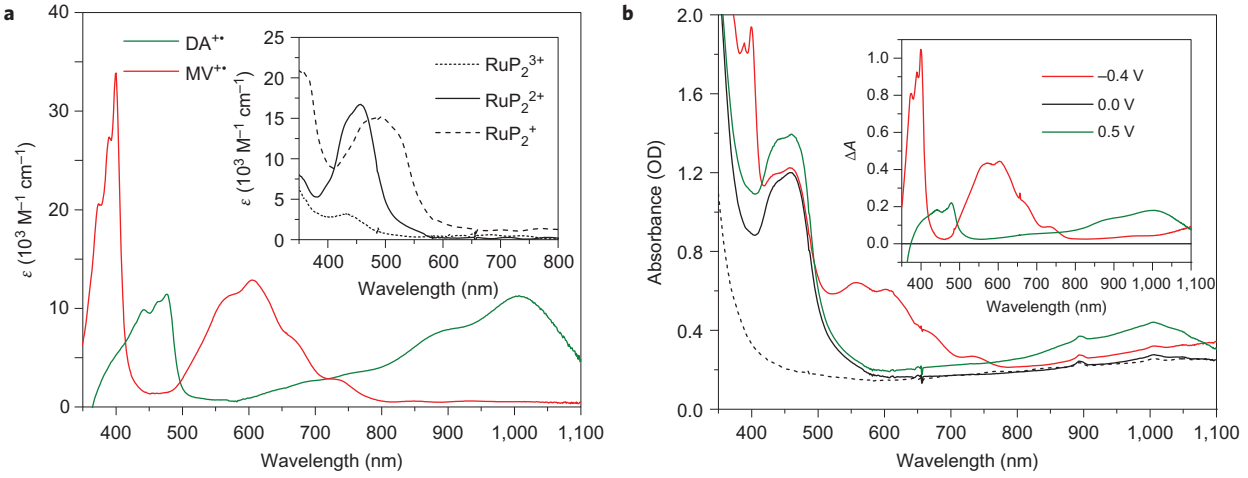

Figure 2 | UV-vis absorptivity and absorbance spectra for individual molecular components and assembled photoanodes, respectively. a, Molar absorptivity spectra for nanoITO|-$MV^{+\bullet}$ and nanoITO|-$DA^{+\bullet}$ in MeCN with 0.1 M $LiClO_4$ obtained from spectroelectrochemical analysis. Spectra for nanoITO|-RuP_2^{3+}, -RuP_2^{2+} and -RuP_2^{+} are shown in the inset. **b**, Absorbance spectra of the photoanode assembly nanoITO|-MV^{2+}-RuP_2^{2+}-DA in MeCN with 0.1 M $LiClO_4$ at E_{app} = –0.4, 0.0 and 0.5 V vs Ag/AgCl (N_2 purged). The background spectrum of the nanoITO electrode is shown as a dashed line. The inset shows absorbance-difference (ΔA) spectra for the indicated applied potentials referenced to 0 V, which indicate that the electron donors and acceptors are still redox active in the full photoanode assembly, as indicated by the oxidation of DA to $DA^{+\bullet}$ at 0.5 V and the reduction of MV^{2+} to $MV^{+\bullet}$ at –0.4 V.

concentration (Γ) was determined to be $\Gamma(RuP_2^{2+}) = 6.5\ (\pm 0.9) \times 10^{-8}$ mol cm^{-2} from multiple electrodes by using the expression $\Gamma = abs_\lambda/(\varepsilon_\lambda 1{,}000)$ with $\lambda = 475$ nm. Decreasing E_{app} from 0 to –0.4 V resulted in a partial reduction of MV^{2+}– to $MV^{+\bullet}$–, as evidenced by the appearance of characteristic absorbance features at 400 and 600 nm (Fig. 2b inset). The appearance of $MV^{+\bullet}$– at the nanoITO interface shows that charge compensation by cation diffusion through the layered assembly is unimpeded on the seconds timescale of the spectroelectrochemical experiment. Long-range oxidation of –DA to $-DA^{+\bullet}$ on the periphery of the assembly was also shown to occur by the growth of absorption features near 450 and 1,000 nm at E_{app} = 0.5 V. Similar spectroelectrochemical data were obtained for the photocathode assembly. Surface concentrations of MV^{2+} and DA in the final assembly structures were determined by spectroelectrochemical changes at applied potentials sufficient for complete reduction or oxidation, respectively.

A summary of surface concentrations in the photoanode and photocathode assemblies is given in Table 2. The ~2:1 ratio for MV^{2+}:RuP_2^{2+} in the photoanode assembly is consistent with a molecular footprint for $-RuP_2^{2+}$–, that is, roughly twice that for MV^{2+}– based on a perpendicular orientation for MV^{2+}– with respect to the nanoITO surface shown in Fig. 1. In the photocathode assembly, the ratio DA:RuP_2^{2+} ≈ 0.8:1 points to a molecular footprint for –DA that is 80% larger than that for $-RuP_2^{2+}$–, also consistent with the perpendicular orientation of –DA shown in Fig. 1. From the data in Table 2, the concentrations of terminal –DA or $-MV^{2+}$ sites are dictated by the surface loading of $-RuP_2^{2+}$– with ~1:1 RuP_2^{2+}:DA and RuP_2^{2+}:MV^{2+} ratios for photoanodes and photocathodes, respectively. Based on these data, the array of assemblies on the nanoITO surface can be viewed as alternating layers of acceptors, chromophores and donors with the member of each layer a component in a molecular triad. Given the dimensions of the individual molecular units, the distance from the nanoITO surface to the terminus of both assemblies is 50–60 Å. The average pore diameter within the mesoscopic nanoITO films is ~360 Å (ref. 40), which ensures a sufficient internal volume for assembly formation.

Table 2 | Surface coverages (Γ, mol cm^{-2}).

	nanoITO|-MV^{2+}-RuP_2^{2+}-DA	nanoITO|-DA-RuP_2^{2+}-MV^{2+}
$\Gamma(MV^{2+})$	$13.7\ (\pm 1.3) \times 10^{-8}$	$8.2\ (\pm 1.8) \times 10^{-8}$
$\Gamma(RuP_2^{2+})$	$6.5\ (\pm 0.9) \times 10^{-8}$	$7.3\ (\pm 0.9) \times 10^{-8}$
Γ(DA)	$6.8\ (\pm 0.2) \times 10^{-8}$	$5.9\ (\pm 0.6) \times 10^{-8}$

Light-driven redox separation in the photoanode assembly. Visible-light-driven redox separation in the photoanode assembly nanoITO|–MV^{2+}–RuP_2^{2+}–DA was investigated by bias-dependent nanosecond transient-absorption measurements. Figure 3a shows transient-absorption-difference spectra obtained at the indicated delay times after 488 nm pulsed-laser excitation in MeCN with 0.1 M $LiClO_4$ at E_{app} = –0.3 V vs Ag/AgCl. Absorption features characteristic of reduced $MV^{+\bullet}$– (400 and 600 nm) and oxidized $-DA^{+\bullet}$ (450 nm) were present at the earliest observation time (50 ns) with no evidence for the initially formed excited-state chromophore ($-RuP_2^{2+*}$–) or its oxidized ($-RuP_2^{3+}$–) or reduced ($-RuP_2^{+}$–) forms. The prompt appearance of $MV^{+\bullet}$– and $-DA^{+\bullet}$ was consistent with a rapid formation of the intra-assembly RS state, nanoITO|–$MV^{+\bullet}$–RuP_2^{2+}–$DA^{+\bullet}$ (equation (1)).

$$\text{nanoITO}|\text{–}MV^{2+}\text{–}RuP_2^{2+}\text{–DA} + h\nu \rightarrow \text{nanoITO}|\text{–}MV^{+\bullet}\text{–}RuP_2^{2+}\text{–}DA^{+\bullet},\ \varphi_{RS1} \quad (1)$$

The appearance of the intra-assembly RS state is consistent with the initial excitation of $-RuP_2^{2+}$– followed by rapid electron-transfer quenching and intra-assembly electron transfer. The details of the individual steps remain to be elucidated by ultrafast transient measurements; however, oxidative and reductive quenching pathways (equations (2) and (3)) are expected to be competitive with $\Delta G^{o\prime} = -0.38$ and –0.35 eV, respectively. The secondary electron-transfer steps needed to form the intra-assembly RS state in equations (2) and (3) are both highly favoured, with $\Delta G^{o\prime} = -0.81$ and –0.84 eV, respectively.

$$\begin{aligned}&\text{nanoITO}|\text{–}MV^{2+}\text{–}RuP_2^{2+*}\text{–DA} \rightarrow\\ &\text{nanoITO}|\text{–}MV^{+\bullet}\text{–}RuP_2^{3+}\text{–DA} \rightarrow\\ &\text{nanoITO}|\text{–}MV^{+\bullet}\text{–}RuP_2^{2+}\text{–}DA^{+\bullet}\end{aligned} \quad (2)$$

$$\begin{aligned}&\text{nanoITO}|\text{–}MV^{2+}\text{–}RuP_2^{2+*}\text{–DA} \rightarrow\\ &\text{nanoITO}|\text{–}MV^{2+}\text{–}RuP_2^{+}\text{–}DA^{+\bullet} \rightarrow\\ &\text{nanoITO}|\text{–}MV^{+\bullet}\text{–}RuP_2^{2+}\text{–}DA^{+\bullet}\end{aligned} \quad (3)$$

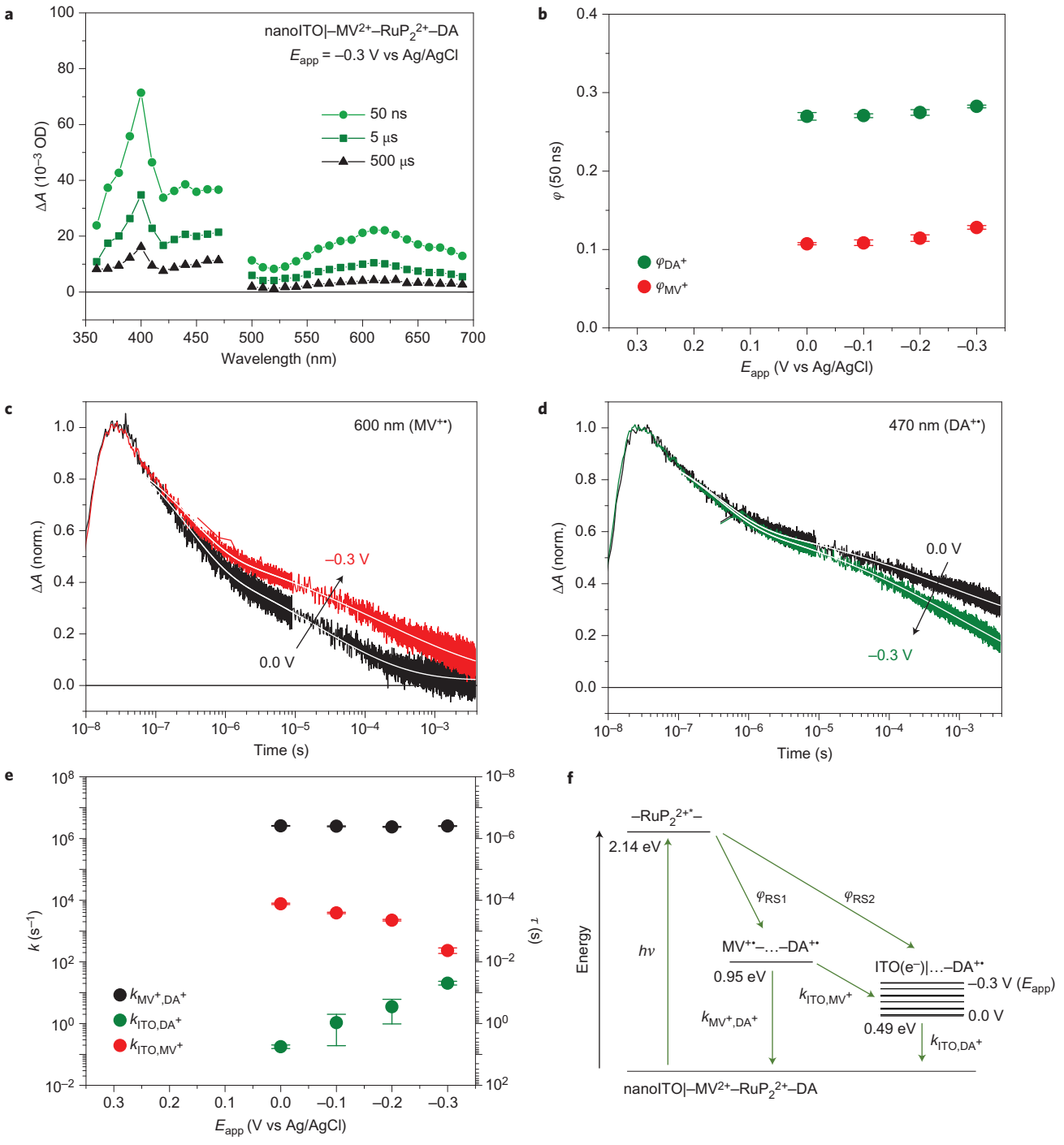

Figure 3 | Summary of bias-dependent transient-absorption measurements on the photoanode assembly nanoITO|-MV^{2+}-RuP_2^{2+}-DA. Measured in MeCN with 0.1 M $LiClO_4$ at room temperature (N_2 purged). **a**, Transient-absorption-difference spectra recorded with E_{app} = –0.3 V vs Ag/AgCl indicate the formation of $MV^{+\bullet}$ and $DA^{+\bullet}$. **b**, Quantum efficiencies for the appearance of $MV^{+\bullet}$ and $DA^{+\bullet}$ measured 50 ns after the laser flash as a function of E_{app}. Error bars represent standard deviation measured over the range 48–52 ns. **c**,**d**, Normalized (norm.) ΔA-time traces at 600 and 470 nm at E_{app} = 0.0 V and –0.3 V with kinetic fits to equation (5). **e**, Kinetic rate constants and lifetimes for k_{MV^+,DA^+}, k_{ITO,DA^+} and k_{ITO,MV^+} as a function of E_{app}. Error bars represent the standard error of the mean rate constant extracted from the kinetic fitting procedure. The bias-independent nature of k_{MV^+,DA^+} is consistent with intra-assembly recombination, whereas the bias-dependent natures of k_{ITO,DA^+} and k_{ITO,MV^+} are consistent with changes in the driving force for electron transfer with the nanoITO electrode. At E_{app} = 0.0 V, k_{ITO,DA^+} = 0.18 s^{-1}, which corresponds to an interfacial RS lifetime of 5.6 s. **f**, Energy diagram that illustrates the formation and decay of the intra-assembly and interfacial RS states for the photoanode assembly.

Quantum efficiencies for the appearance of $MV^{+\bullet}$ and $DA^{+\bullet}$ (φ_{MV^+} and φ_{DA^+}) were determined from transient-absorption amplitude changes recorded 50 ns after the laser pulse. As shown by the results in Fig. 3b and Supplementary Table 3, φ_{MV^+} and φ_{DA^+} were relatively constant at 0.12 ± 0.01 and 0.27 ± 0.01, respectively, and independent of the applied potential from E_{app} = –0.3 to 0.0 V. Experiments on the redox-inert mesoporous oxide ZrO_2 showed that excited-state quenching occurred with an efficiency of 97% (Supplementary Fig. 8). Therefore, the low φ_{MV^+} and φ_{DA^+} are probably caused by back-electron- transfer reactions (that is, $MV^{+\bullet}$–RuP_2^{3+}–DA → MV^{2+}–RuP_2^{2+}–DA and

MV^{2+}–RuP_2^{+}–$DA^{+\bullet}$ → MV^{2+}–RuP_2^{2+}–DA), in competition with the formation of the intra-assembly RS state.

The ratio $\varphi_{MV^+}/\varphi_{DA^+} < 1$ can be attributed to the transfer of some fraction of the photoproduced reductive equivalents to the nanoITO electrode to give the interfacial RS state, nanoITO(e^-)|–MV^{2+}–RuP_2^{2+}–$DA^{+\bullet}$, presumably formed by electron transfer from –$RuP_2^{2+\star}$–, –RuP_2^{+}– or $MV^{+\bullet}$ on a timescale <50 ns (equation (4); see the Supplementary Information for further discussion). With this interpretation, $\varphi_{RS1} = \varphi_{MV^+} = 0.12$ is the efficiency of formation of the intra-assembly RS state at 50 ns and $\varphi_{RS2} = \varphi_{DA^+} - \varphi_{MV^+} = 0.15$ is the efficiency of formation of the interfacial RS state at 50 ns. The total efficiency for the redox separation, $\varphi_{RS1} + \varphi_{RS2} = 0.27$, is similar to solution-based values for donor–chromophore–acceptor molecular triads based on $[Ru^{II}(bpy)_3]^{2+}$ chromophores and similar donors and/or acceptors previously reported in the literature ($\varphi = 0.25$–0.26)[41,42].

$$\text{nanoITO}|\text{–}MV^{2+}\text{–}RuP_2^{2+}\text{–DA} + h\nu \rightarrow \text{nanoITO}(e^-)|\text{–}MV^{2+}\text{–}RuP_2^{2+}\text{–}DA^{+\bullet},\ \varphi_{RS2} \quad (4)$$

Figure 3c,d shows single-wavelength ΔA–time traces at 600 and 470 nm, wavelengths dominated by $MV^{+\bullet}$– and –$DA^{+\bullet}$, respectively. The transients at both wavelengths persisted for milliseconds or longer and underwent non-exponential bimodal decay kinetics with short and long time components. The ΔA–time data at 600 and 470 nm were fit to the sum of two Kolrausch–Williams–Watts (KWW) stretched exponential functions with the decay kinetics described as distributions of first-order processes (equation (5)). The KWW function has been used to characterize highly dispersive kinetics, including electron transfer at semiconductor/solution interfaces in dye-sensitized solar cells and within polymer matrices[29,30,43–45]. In equation (5), k_1 and k_2 are characteristic rate constants, and β_1 and β_2 are parameters that describe the distribution width. Average rate constants, $\langle k_1 \rangle$ and $\langle k_2 \rangle$, were calculated as the first moment of the distribution functions, as shown in equation (6), where Γ is the Gamma function. Kinetic fits are shown in Fig. 3c,d and fitting parameters are listed in Supplementary Tables 4 and 5.

$$\Delta A(t) = \Delta A_1 \exp(-(k_1 t)^{\beta_1}) + \Delta A_2 \exp(-(k_2 t)^{\beta_2}) \quad (5)$$

$$\langle k_i \rangle = k_i \beta_i / \Gamma(1/\beta_i) \quad (6)$$

For the short time component (50 ns to 1 μs), the average rate constants derived from 600 and 470 nm decays were the same within experimental error and independent of the applied potential to give $\langle k_1 \rangle = 2.5\ (\pm 0.4) \times 10^6\ s^{-1}$. This observation was consistent with a back-electron transfer of the intra-assembly RS state, shown in equation (7), such that $\langle k_1 \rangle = k_{MV^+,DA^+}$. The lifetime of the intra-assembly RS state was therefore $\tau = 1/k_{MV^+,DA^+} = 400$ ns.

$$\text{nanoITO}|\text{–}MV^{+\bullet}\text{–}RuP_2^{2+}\text{–}DA^{+\bullet} \rightarrow \text{nanoITO}|\text{–}MV^{2+}\text{–}RuP_2^{2+}\text{–DA},\ k_{MV^+,DA^+} \quad (7)$$

$$\text{nanoITO}|\text{–}MV^{+\bullet}\text{–}RuP_2^{2+}\text{–}DA^{+\bullet} \rightarrow \text{nanoITO}(e^-)|\text{–}MV^{2+}\text{–}RuP_2^{2+}\text{–}DA^{+\bullet},\ k_{ITO,MV^+} \quad (8)$$

$$\text{nanoITO}(e^-)|\text{–}MV^{2+}\text{–}RuP_2^{2+}\text{–}DA^{+\bullet} \rightarrow \text{nanoITO}|\text{–}MV^{2+}\text{–}RuP_2^{2+}\text{–DA},\ k_{ITO,DA^+} \quad (9)$$

For the long time component (>1 μs), there was a noticeable bias dependence on the decay kinetics of 600 and 470 nm, attributed to changes in driving force for the $MV^{+\bullet}$ → nanoITO (k_{ITO,MV^+}) and nanoITO(e^-) → $DA^{+\bullet}$ (k_{ITO,DA^+}) electron-transfer reactions shown in equations (8) and (9), respectively. The average rate constants for 600 nm ($\langle k_2 \rangle = k_{ITO,MV^+}$) and 470 nm ($\langle k_2 \rangle = k_{ITO,DA^+}$) are plotted against E_{app} in Fig. 3e. Here k_{ITO,MV^+} increased exponentially from 240 s^{-1} (–0.3 V) to 7,600 s^{-1} (0.0 V), which corresponds to a change in driving force from $\Delta G^{o\prime} = -0.16$ to –0.46 eV, respectively. These values are surprisingly small given that the quantum efficiencies at 50 ns are consistent with a rapid electron transfer from the assembly to the nanoITO electrode. The origin of rapid electron transfer is not clear, but may arise by direct electron transfer from reduced –RuP_2^{+}– or excited-state –$RuP_2^{2+\star}$–, or fast electron transfer by $MV^{+\bullet}$– components present in a unique chemical environment that favours this process.

Over the same potential range, k_{ITO,DA^+} decreased from 21 s^{-1} (–0.3 V) to 0.18 s^{-1} (0.0 V) with $\Delta G^{o\prime} = -0.79$ and –0.49 eV, respectively, consistent with a slower long-range nanoITO(e^-) → $DA^{+\bullet}$ back-electron transfer. The driving-force dependence of the latter is remarkable, and results in an average interfacial RS lifetime of $\tau = 1/k_{ITO,DA^+} = 5.6$ s at 0 V. At $E_{app} > 0.0$ V, the slow loss of $DA^{+\bullet}$ led to a steady-state increase in background $DA^{+\bullet}$ with each laser pulse, which precludes the collection of reliable transient data. The slow kinetics for nanoITO(e^-) → $DA^{+\bullet}$ back-electron transfer is a consequence of the long distance (50–60 Å) for the reaction and the electronically decoupled Zr^{IV}–phosphonate linkages. For comparison, the distance for inhibited back-electron transfer in photosystem II between reduced plastoquinone and the oxidized water-evolving complex is ~70 Å (ref. 46). The energy diagram in Fig. 3f summarizes the dynamic events that occur after the formation and decay of the intra-assembly and interfacial RS states as a function of E_{app}.

Light-driven redox separation in the photocathode assembly. Figure 4a shows transient-absorption-difference spectra obtained at the indicated delay times after a 488 nm excitation of the photocathode assembly nanoITO|–DA–RuP_2^{2+}–MV^{2+} at $E_{app} = -0.3$ V in MeCN with 0.1 M $LiClO_4$. Laser-flash excitation resulted in the appearance of the intra-assembly RS state nanoITO|–$DA^{+\bullet}$–RuP_2^{2+}–$MV^{+\bullet}$ (equation (10)), with both $MV^{+\bullet}$ and $DA^{+\bullet}$ observed at the earliest observation time with comparable efficiencies of $\varphi_{MV^+} = 0.32$ and $\varphi_{DA^+} = 0.23$. As the applied potential was adjusted towards positive values, φ_{MV^+} remained nearly constant, whereas φ_{DA^+} increased to be equal with $\varphi_{MV^+} \approx 0.30$ at the most-positive potential of $E_{app} = 0.3$ V (Fig. 4b and Supplementary Table 3). The ratio $\varphi_{MV^+}/\varphi_{DA^+} > 1$ at negative potentials points to partial electron transfer from nanoITO to –$RuP_2^{2+\star}$–, –RuP_2^{3+}– or $DA^{+\bullet}$– within 50 ns of the laser pulse to give the interfacial RS state nanoITO(h^+)|–DA– RuP_2^{2+}–$MV^{+\bullet}$ (equation (11); see the Supplementary Information for further discussion). Based on these data, the quantum efficiency for the formation of the intra-assembly RS state at $E_{app} = -0.3$ V is $\varphi_{RS1} = \varphi_{DA^+} = 0.23$ and for the interfacial RS state it is $\varphi_{RS2} = \varphi_{MV^+} - \varphi_{DA^+} = 0.09$. The total redox-separation efficiency ($\varphi_{RS1} + \varphi_{RS2}$) was constant at 0.31 ± 0.01 over the range of E_{app} and similar to that found for the photoanode assembly.

$$\text{nanoITO}|\text{–DA–}RuP_2^{2+}\text{–}MV^{2+} + h\nu \rightarrow \text{nanoITO}|\text{–}DA^{+\bullet}\text{–}RuP_2^{2+}\text{–}MV^{+\bullet},\ \varphi_{RS1} \quad (10)$$

$$\text{nanoITO}|\text{–DA–}RuP_2^{2+}\text{–}MV^{2+} + h\nu \rightarrow \text{nanoITO}(h^+)|\text{–DA–}RuP_2^{2+}\text{–}MV^{+\bullet},\ \varphi_{RS2} \quad (11)$$

Figure 4c,d shows normalized single wavelength ΔA–time traces monitored at 600 and 470 nm. As with the photoanode assembly, decay occurred with bimodal kinetics with a bias-independent short time component and a bias-dependent long time component. Kinetic fits to equation (5) are overlaid on the data with fitting

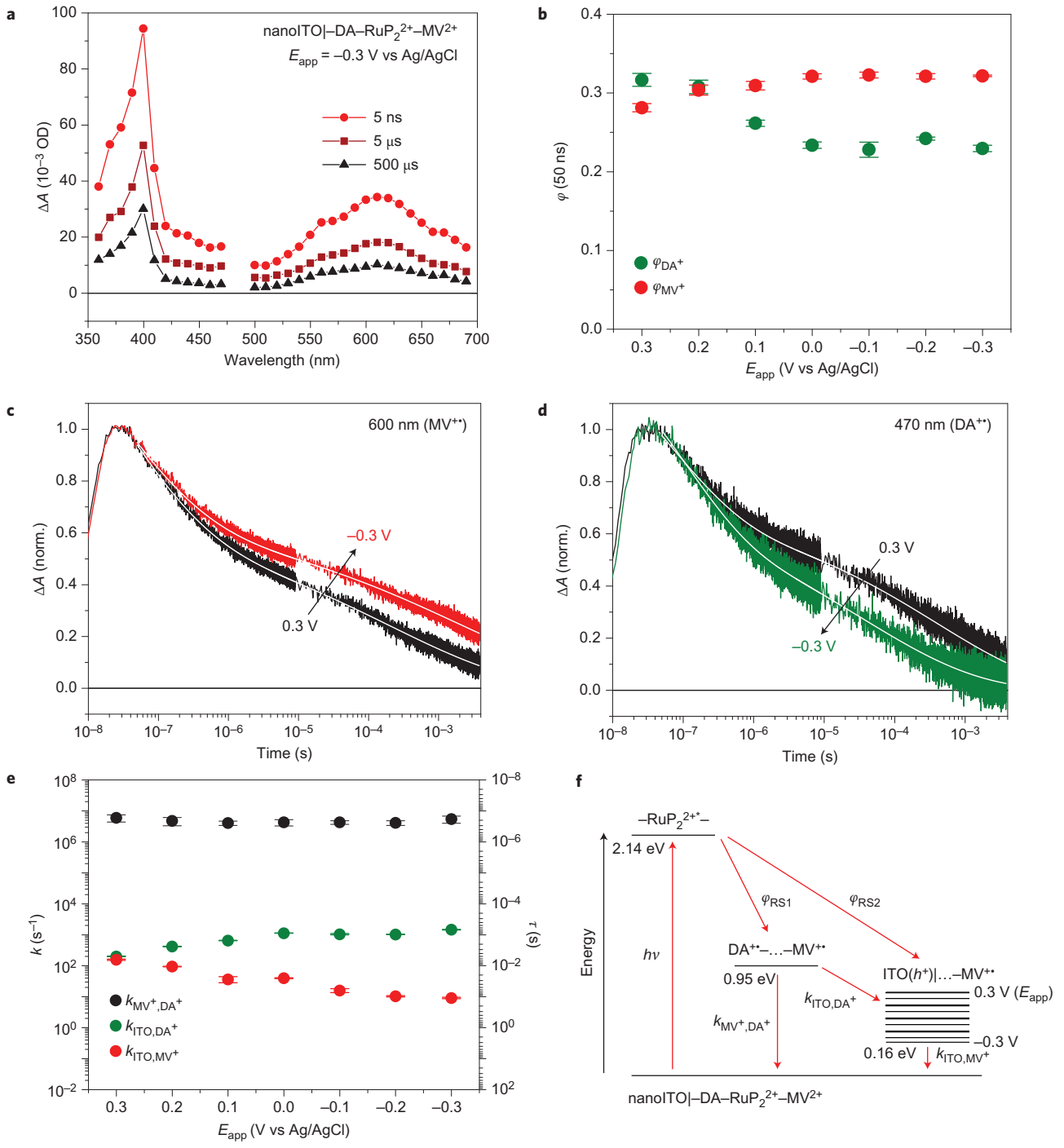

Figure 4 | Summary of bias-dependent transient-absorption measurements on the photocathode assembly nanoITO|-DA-RuP_2^{2+}-MV^{2+}. Measured in MeCN with 0.1 M $LiClO_4$ at room temperature (N_2 purged). **a**, Transient-absorption-difference spectra recorded with E_{app} = –0.3 V vs Ag/AgCl show the formation of $MV^{+\bullet}$ and $DA^{+\bullet}$. **b**, Quantum efficiencies for the appearance of $MV^{+\bullet}$ and $DA^{+\bullet}$ measured 50 ns after the laser flash as a function of E_{app}. Error bars represent the standard deviation measured over the range 48–52 ns. **c**,**d**, Normalized ΔA-time traces at 600 and 470 nm at E_{app} = 0.0 and –0.3 V show kinetic fits to equation (5). **e**, Rate constants and lifetimes for k_{MV^+,DA^+}, k_{ITO,DA^+} and k_{ITO,MV^+} as a function of E_{app}. Error bars represent the standard error of the mean rate constant extracted from the kinetic fitting procedure. The bias-independent nature of k_{MV^+,DA^+} is consistent with intra-assembly recombination, whereas the bias-dependent natures of k_{ITO,DA^+} and k_{ITO,MV^+} are consistent with changes in the driving force for electron transfer with the nanoITO electrode. At E_{app} = 0.0 V, k_{ITO,MV^+} = 39 s^{-1}, which corresponds to an interfacial RS lifetime of 26 ms. **f**, Energy diagram that illustrates the formation and decay of the intra-assembly and interfacial RS states for the photocathode assembly.

parameters listed in Supplementary Tables 6 and 7. From these data, the kinetics of the short time component were independent of the monitoring wavelength and applied potential, consistent with back-electron transfer of the intra-assembly RS state (equation (12)). Analysis of the data gave $\langle k_1 \rangle = k_{MV^+,DA^+} = 4.6\ (\pm 0.9) \times 10^6\ s^{-1}$, comparable to $k_{MV^+,DA^+} = 2.5\ (\pm 0.4) \times 10^6\ s^{-1}$ obtained for the

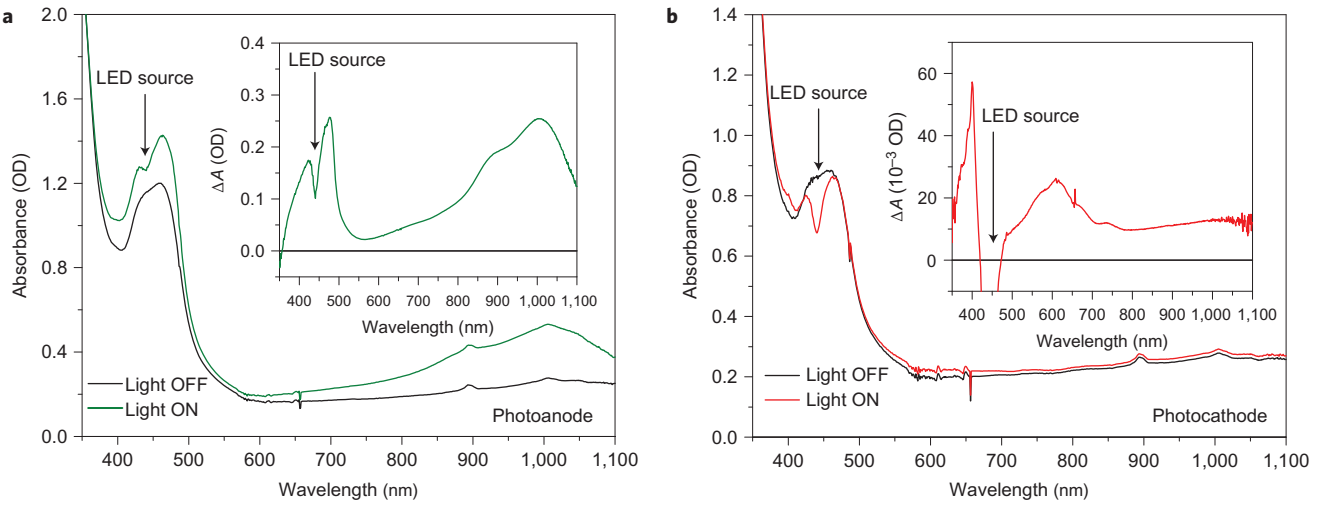

Figure 5 | Steady-state photolysis of photoanode and photocathode assemblies. a,**b**, UV-vis absorbance spectra for the photoanode (**a**) and photocathode (**b**) assemblies in the dark and under illumination by a 455 nm LED (52 mW cm^{-2}) at E_{app} = 0.0 V vs Ag/AgCl in MeCN with 0.1 M $LiClO_4$ (N_2 purged). The interfacial RS states nanoITO(e^-)|-MV^{2+}-RuP_2^{2+}-$DA^{+\bullet}$ (photoanode) and nanoITO(h^+)|-DA-RuP_2^{2+}-$MV^{+\bullet}$ (photocathode) are clearly observed in the difference spectra shown in the insets. Time-resolved changes to the absorbance spectra are shown in Supplementary Fig. 12.

photoanode assembly under the same conditions.

$$\text{nanoITO}|\text{–DA}^{+\bullet}\text{–RuP}_2^{2+}\text{–MV}^{+\bullet} \rightarrow \text{nanoITO}|\text{–DA–RuP}_2^{2+}\text{–MV}^{2+},\ k_{MV^+,DA^+} \quad (12)$$

$$\text{nanoITO}|\text{–DA}^{+\bullet}\text{–RuP}_2^{2+}\text{–MV}^{+\bullet} \rightarrow \text{nanoITO}(h^+)|\text{– DA–RuP}_2^{2+}\text{– MV}^{+\bullet},\ k_{ITO,DA^+} \quad (13)$$

$$\text{nanoITO}(h^+)|\text{–DA–RuP}_2^{2+}\text{–MV}^{+\bullet} \rightarrow \text{nanoITO}|\text{– DA–RuP}_2^{2+}\text{–MV}^{2+},\ k_{ITO,MV^+} \quad (14)$$

Figure 3e shows the average rate constants associated with the long time components for $DA^{+\bullet}$ monitored at 470 nm ($<k_2> = k_{ITO,DA^+}$) and for $MV^{+\bullet}$ monitored at 600 nm ($<k_2> = k_{ITO,MV^+}$) (equations (13) and (14)). From these data, k_{ITO,DA^+} decreased from 1,400 s^{-1} (–0.3 V) to 200 s^{-1} (0.3 V), similar to the driving-force dependence observed for back-electron transfer in the photoanode assembly. Likewise, k_{ITO,MV^+} increased with E_{app}, consistent with the expected driving-force dependence for interfacial back-electron transfer in equation (14). At E_{app} = 0.0 V, k_{ITO,MV^+} = 39 s^{-1} with an interfacial RS state lifetime of 26 ms and increased to 110 ms (k_{ITO,MV^+} = 8.9 s^{-1}) at –0.3 V.

In previous studies on chromophores bound directly to nanoITO, back-electron transfer was shown to occur on the picoseconds-to-microseconds timescale[15–18,47]. The remarkably long-lived interfacial RS states for the photoanode nanoITO(e^-)|-MV^{2+}-RuP_2^{2+}-$DA^{+\bullet}$ and the photocathode nanoITO(h^+)|-DA-RuP_2^{2+}-$MV^{+\bullet}$ assemblies reported here result from the long-range nature of the back-electron-transfer processes and the electronically decoupled Zr^{IV}–phosphonate linkages. Although detailed mechanisms for RS state recombination are still under investigation, the net result is an ultra-slow intramolecular back-electron transfer with lifetimes of 5.6 s for the photoanode and 26 ms for the photocathode at E_{app} = 0.0 V vs Ag/AgCl. The timescale for back-electron transfer in the photoanode assembly is comparable to that of interfacial RS states of dye-sensitized TiO_2 electrodes[29,30], whereas that of the photocathode is far slower than any previous reports of interfacial RS states at dye-sensitized p-type metal oxides, such as NiO[32–36].

Light-driven RS lifetimes that extend into the milliseconds-to-seconds timescale are important to achieve steady-state populations of oxidized and reduced catalysts for dye-sensitized photoelectrosynthesis cells that drive photoanodic H_2O oxidation and photocathodic CO_2/H^+ reduction. As a proof-of-principle experiment, the photoelectrodes reported here were exposed to constant visible-light illumination (455 nm light-emitting diode (LED)) with E_{app} = 0.0 V vs Ag/AgCl to see if oxidized $DA^{+\bullet}$ and reduced $MV^{+\bullet}$ could be stored under steady-state conditions. Figure 5 shows UV-vis absorbance spectra for the photoanode and photocathode assemblies, from which visible-light illumination clearly resulted in spectral changes associated with oxidized $DA^{+\bullet}$ and reduced $MV^{+\bullet}$, respectively.

Conclusion

Our results are important as they highlight an interfacial molecular p/n junction strategy applicable to solar-to-electrical and solar-to-fuel dye-sensitized photoelectrochemical cells. This strategy is based on a modular layer-by-layer approach that allows for the incorporation of light absorbers, electron-transfer mediators and catalysts by a simple dipping procedure. A key element is the use of the high-surface-area transparent conducting oxide, nanoITO, which participates as an optically transparent redox-active element and plays a significant role in achieving long lifetimes for redox separation; 5.6 s for the photoanode and 26 ms for the photocathode at E_{app} = 0.0 V vs Ag/AgCl. We are currently extending this modular strategy to assemblies with molecular catalysts for H_2O oxidation and CO_2/H^+ reduction.

Methods

All the synthetic and experimental details are included in the Supplementary Information.

Received 23 November 2015; accepted 26 April 2016; published online 6 June 2016

References

1. Shockley, W. & Queisser, H. J. Detailed balance limit of efficiency of p–n junction solar cells. *J. Appl. Phys.* **32,** 510–519 (1961).
2. Meyer, T. J. Chemical approaches to artificial photosynthesis. *Acc. Chem. Res.* **22,** 163–170 (1989).
3. Alstrum-Acevedo, J. H., Brennaman, M. K. & Meyer, T. J. Chemical approaches to artificial photosynthesis. 2. *Inorg. Chem.* **44,** 6802–6827 (2005).
4. Chakraborty, S., Wadas, T. J., Hester, H., Schmehl, R. & Eisenberg, R. Platinum chromophore-based systems for photoinduced charge separation: a molecular design approach for artificial photosynthesis. *Inorg. Chem.* **44,** 6865–6878 (2005).

5. Kaschak, D. M., Johnson, S. A., Waraksa, C. C., Pogue, J. & Mallouk, T. E. Artificial photosynthesis in lamellar assemblies of metal poly(pyridyl) complexes and metalloporphyrins. *Coord. Chem. Rev.* **186,** 403–416 (1999).
6. Wasielewski, M. R. Photoinduced electron transfer in supramolecular systems for artificial photosynthesis. *Chem. Rev.* **92,** 435–461 (1992).
7. Gust, D. *et al.* Efficient multistep photoinitiated electron transfer in a molecular pentad. *Science* **248,** 199–201 (1990).
8. Gust, D. & Moore, T. A. Mimicking photosynthesis. *Science* **244,** 35–41 (1989).
9. Moore, T. A. *et al.* Photodriven charge separation in a carotenoporphyrin–quinone triad. *Nature* **307,** 630–632 (1984).
10. Yonemoto, E. H., Riley, R. L., Atherton, S. J., Schmehl, R. H. & Mallouk, T. E. Photoinduced electron transfer in covalently linked ruthenium tris(bipyridyl)–viologen molecules: observation of back electron transfer in the Marcus inverted region. *J. Am. Chem. Soc.* **114,** 8081–8087 (1992).
11. Sherman, B. D. *et al.* Evolution of reaction center mimics to systems capable of generating solar fuel. *Photosynth. Res.* **120,** 59–70 (2014).
12. Massari, A. M. *et al.* Ultrathin micropatterned porphyrin films assembled via zirconium phosphonate chemistry. *Polyhedron* **22,** 3065–3072 (2003).
13. Imahori, H. *et al.* Light-harvesting and photocurrent generation by gold electrodes modified with mixed self-assembled monolayers of boron–dipyrrin and ferrocene–porphyrin–fullerene triad. *J. Am. Chem. Soc.* **123,** 100–110 (2001).
14. Vermeulen, L. A., Snover, J. L., Sapochak, L. S. & Thompson, M. E. Efficient photoinduced charge separation in layered zirconium viologen phosphonate compounds. *J. Am. Chem. Soc.* **115,** 11767–11774 (1993).
15. Farnum, B. H., Nakada, A., Ishitani, O. & Meyer, T. J. Bias-dependent oxidative or reductive quenching of a molecular excited-state assembly bound to a transparent conductive oxide. *J. Phys. Chem. C* **119,** 25180–25187 (2015).
16. Farnum, B. H., Morseth, Z. A., Brennaman, M. K., Papanikolas, J. M. & Meyer, T. J. Driving force dependent, photoinduced electron transfer at degenerately doped, optically transparent semiconductor nanoparticle interfaces. *J. Am. Chem. Soc.* **136,** 15869–15872 (2014).
17. Farnum, B. H., Morseth, Z. A., Brennaman, M. K., Papanikolas, J. M. & Meyer, T. J. Application of degenerately doped metal oxides in the study of photoinduced interfacial electron transfer. *J. Phys. Chem. B* **119,** 7698–7711 (2015).
18. Farnum, B. H. *et al.* Photoinduced interfacial electron transfer within a mesoporous transparent conducting oxide film. *J. Am. Chem. Soc.* **136,** 2208–2211 (2014).
19. Hoertz, P. G., Chen, Z., Kent, C. A. & Meyer, T. J. Application of high surface area tin-doped indium oxide nanoparticle films as transparent conducting electrodes. *Inorg. Chem.* **49,** 8179–8181 (2010).
20. Chen, Z. *et al.* Nonaqueous catalytic water oxidation. *J. Am. Chem. Soc.* **132,** 17670–17673 (2010).
21. Fang, M., Kaschak, D. M., Sutorik, A. C. & Mallouk, T. E. A 'mix and match' ionic–covalent strategy for self-assembly of inorganic multilayer films. *J. Am. Chem. Soc.* **119,** 12184–12191 (1997).
22. Kaschak, D. M. *et al.* Photoinduced energy and electron transfer reactions in lamellar polyanion/polycation thin films: toward an inorganic 'leaf'. *J. Am. Chem. Soc.* **121,** 3435–3445 (1999).
23. Ishida, T. *et al.* Self-assembled monolayer and multilayer formation using redox-active Ru complex with phosphonic acids on silicon oxide surface. *Appl. Surf. Sci.* **255,** 8824–8830 (2009).
24. Akatsuka, K. *et al.* Photoelectrochemical properties of alternating multilayer films composed of titania nanosheets and Zn porphyrin. *Langmuir* **23,** 6730–6736 (2007).
25. Katz, H. E. Multilayer deposition of novel organophosphonates with zirconium (IV). *Chem. Mater.* **6,** 2227–2232 (1994).
26. Ungashe, S. B., Wilson, W. L., Katz, H. E., Scheller, G. R. & Putvinski, T. M. Synthesis, self-assembly, and photophysical dynamics of stacked layers of porphyrin and viologen phosphonates. *J. Am. Chem. Soc.* **114,** 8717–8719 (1992).
27. Nayak, A. *et al.* Synthesis and photophysical characterization of porphyrin and porphyrin–Ru(II) polypyridyl chromophore–catalyst assemblies on mesoporous metal oxides. *Chem. Sci.* **5,** 3115–3119 (2014).
28. Hanson, K. *et al.* Self-assembled bilayer films of ruthenium(II)/polypyridyl complexes through layer-by-layer deposition on nanostructured metal oxides. *Angew. Chem. Int. Ed.* **51,** 12782–12785 (2012).
29. Ardo, S. & Meyer, G. J. Photodriven heterogeneous charge transfer with transition-metal compounds anchored to TiO_2 semiconductor surfaces. *Chem. Soc. Rev.* **38,** 115–164 (2009).
30. Hagfeldt, A., Boschloo, G., Sun, L., Kloo, L. & Pettersson, H. Dye-sensitized solar cells. *Chem. Rev.* **110,** 6595–6663 (2010).
31. Knauf, R. R., Kalanyan, B., Parsons, G. N. & Dempsey, J. L. Charge recombination dynamics in sensitized SnO_2/TiO_2 core/shell photoanodes. *J. Phys. Chem. C* **119,** 28353–28360 (2015).
32. Nattestad, A. *et al.* Highly efficient photocathodes for dye-sensitized tandem solar cells. *Nature Mater.* **9,** 31–35 (2010).
33. Weidelener, M. *et al.* Synthesis and characterization of perylene–bithiophene–triphenylamine triads: studies on the effect of alkyl-substitution in p-type NiO based photocathodes. *J. Mater. Chem.* **22,** 7366–7379 (2012).
34. Gibson, E. A. *et al.* A p-type NiO-based dye-sensitized solar cell with an open-circuit voltage of 0.35 V. *Angew. Chem. Int. Ed.* **48,** 4402–4405 (2009).
35. Warnan, J. *et al.* Multichromophoric sensitizers based on squaraine for NiO based dye-sensitized solar cells. *J. Phys. Chem. C* **118,** 103–113 (2014).
36. Zhang, L. *et al.* Long-lived charge separated state in NiO-based p-type dye-sensitized solar cells with simple cyclometalated iridium complexes. *J. Phys. Chem. Lett.* **5,** 2254–2258 (2014).
37. Felderhoff, M., Heinen, S., Molisho, N., Webersinn, S. & Walder, L. Molecular suppression of the pimerization of viologens attached to nanocrystalline titanium dioxide thin-film electrodes. *Helv. Chim. Acta* **83,** 181–192 (2000).
38. Hanson, K. *et al.* Structure–property relationships in phosphonate-derivatized, Ru(II) polypyridyl dyes on metal oxide surfaces in an aqueous environment. *J. Phys. Chem. C* **116,** 14837–14847 (2012).
39. Watanabe, T. & Honda, K. Measurement of the extinction coefficient of the methyl viologen cation radical and the efficiency of its formation by semiconductor photocatalysis. *J. Phys. Chem.* **86,** 2617–2619 (1982).
40. Lapides, A. M. *et al.* Synthesis, characterization, and water oxidation by a molecular chromophore–catalyst assembly prepared by atomic layer deposition. The 'mummy' strategy. *Chem. Sci.* **6,** 6398–6406 (2015).
41. Danielson, E., Elliott, C. M., Merkert, J. W. & Meyer, T. J. Photochemically induced charge separation at the molecular level. A chromophore quencher complex containing both an electron transfer donor and an acceptor. *J. Am. Chem. Soc.* **109,** 2519–2520 (1987).
42. Treadway, J. A., Chen, P., Rutherford, T. J., Keene, F. R. & Meyer, T. J. Mapping electron transfer pathways in a chromophore–quencher triad. *J. Phys. Chem. A* **101,** 6824–6826 (1997).
43. Nelson, J. Continuous-time random-walk model of electron transport in nanocrystalline TiO_2 electrodes. *Phys. Rev. B* **59,** 374–380 (1999).
44. Lindsey, C. P. & Patterson, G. D. Detailed comparison of the Williams–Watts and Cole–Davidson functions. *J. Chem. Phys.* **73,** 3348–3357 (1980).
45. Williams, G. & Watts, D. C. Non-symmetrical dielectric relaxation behaviour arising from a simple empirical decay function. *Trans. Faraday Soc.* **66,** 80–85 (1969).
46. Ferreira, K. N., Iverson, T. M., Maghlaoui, K., Barber, J. & Iwata, S. Architecture of the photosynthetic oxygen-evolving center. *Science* **303,** 1831–1838 (2004).
47. Huang, Z. *et al.* Dye-controlled interfacial electron transfer for high-current indium tin oxide photocathodes. *Angew. Chem. Int. Ed.* **54,** 6857–6861 (2015).

Acknowledgements

This material is based on work supported by the US Department of Energy, Office of Science, Office of Basic Energy Sciences, under Award No. DE-FG02-06ER15788.

Author contributions

B.H.F. and T.J.M. conceived and designed the experiments. K.R.W. synthesized the molecular species. B.H.F. assembled the electrodes and performed the transient-absorption and photolysis experiments. B.H.F. and T.J.M. wrote the paper.

Additional information

Supplementary information is available in the online version of the paper. Reprints and permissions information is available online at www.nature.com/reprints. Correspondence and requests for materials should be addressed to T.J.M.

Competing financial interests

The authors declare no competing financial interests.